RESEARCH

Stability of a lined rock cavern for compressed air energy storage containing a weak interlayer during blasting in the adjacent cavern: model tests and numerical simulation

Mengchen Zhang · Yi Luo · Hangli Gong · Xin Liu · Yunchen Deng

Abstract To evaluate the stability of a lined rock cavern (LRC) for compressed air energy storage (CAES) containing a weak interlayer during blasting in the adjacent cavern, a newly excavated tunnel-type LRC was taken as the research object. By combining similar model tests and numerical simulation, the dynamic responses and deformation characteristics of the LRC for CAES under joint action of factors including the gas storage pressure, weak interlayer, and blast load were studied. The influences of the thickness, dip angle, and location of the weak interlayer on deformation of the LRC were discussed. The results show that as the gas storage pressure increases, the rate of change in strains in regions of the LRC near the weak interlayer is accelerated, and the gas storage pressure more significantly influences the sealing layer and lining than the surrounding rocks. The presence of the weak interlayer causes stress concentration in the LRC and increases the circumferential strain and residual strain of the LRC. Under the blast load, the right-side wall of the LRC shows the poorest stability, and the presence of the weak interlayer results in the energy loss in the propagation process of stress waves and an increment of peak strain in regions of the LRC around the interlayer. When the weak interlayer is separated from the LRC, as the thickness of the weak interlayer increases, the confinement of surrounding rocks at the interlayer on the LRC reduces and the circumferential strain increases. As the dip angle of the interlayer increases, the peak strain in the right upper side of the LRC grows significantly. As the distance from the weak interlayer to the LRC boundary increases, the circumferential strain in regions of the LRC near the interlayer decreases significantly. If the distance is less than $0.2r$, the increment of the distance significantly affects the peak strain.

1 Introduction

Compressed air energy storage (CAES) is a large-scale energy storage technique that has become more popular in recent years. It entails the use of superfluous energy to drive compressors to compress air and store in underground storage and then pumping the

M. Zhang · Y. Luo · H. Gong (✉)
Sanya Science and Education Innovation Park, Wuhan University of Technology, Sanya 572024, China
e-mail: hangligong58@whut.edu.cn

M. Zhang · Y. Luo · H. Gong · X. Liu · Y. Deng
School of Civil Engineering and Architecture, Wuhan University of Technology, Wuhan 430070, China

Y. Luo
Hubei Key Laboratory of Roadway Bridge and Structure Engineering, Wuhan University of Technology, Wuhan 430070, China

compressed air out of underground storage to turbines for power generation when needed (Mahlia et al. 2014; Geissbühler et al. 2018; Yu et al. 2022). CAES power plants are generally built in geological media including hard-rock caverns of high stability, underground salt beds, depleted oil and gas reservoirs, and abandoned mines (Chen and Wang 2022; Han et al. 2021; Sopher et al. 2019; Carranza-Torres et al. 2017). The tunnel-type lined rock caverns (LRCs) for CAES formed by excavation and support of hard rocks are composed of three parts, namely, the sealing layer (for air-tightness), a concrete lining, and the surrounding rock (Zhou et al. 2018; Yang et al. 2021). The overall stability of LRCs is a key factor in ensuring the safe and stable operation of CAES systems. Additionally, tunnel-type LRCs for CAES are generally built in deep abandoned roadways under complex geological conditions, where the weak interlayers such as joints and faults in the complex geological bodies exert critical influences on the stability of LRCs. Besides, they are easily affected by the strong dynamic disturbances induced by blasting excavation in adjacent engineering operations (Wang et al. 2022a, b, c; Saedi et al. 2021; Zhao et al. 2018; Xie et al. 2022). Therefore, studying the stability of LRCs for CAES under the joint action of blast loads and weak interlayers is of important theoretical and practical significance.

LRCs for CAES reconstructed from abandoned spaces are generally shown as tunnels and the overall stability of the lining is a key factor that ensures safe and stable operation of the CAES system (Li et al. 2023a, b; Rutqvist et al. 2012; Xue et al. 2021). Considering internal factors including structural performance of lining and internal gas storage state that affect stability of the LRC for CAES, Wang et al. (2018a, b) found that, if the internal pressure drops too fast, the load on the top of the LRC cannot be timeously transferred and thus forms a zone of stress-concentration, causing local damage to the top of the LRC. Zhang et al. (2017a, b) found that too rapid a gas-storage rate and the loss of gas pressure both aggravate deformation of surrounding rocks. Kim et al. (2013) believed that the possibility of tensile failure of LRCs can be reduced if the excavation-damaged zone is small and a flexible concrete lining is used. Jiang et al. (2023) believe that the fracture width in the lining can be controlled if using appropriate lining reinforcement

methods and improving the quality of surrounding rocks. Kim et al. (2012) showed that the temperature, stress, and deformation of structures including the sealing layer, lining, and rocks surrounding underground LRCs for CAES all change correspondingly in the substantial heating and pressurizing process and cooling and depressurizing process of compressed air. Generally speaking, the internal pressure, gas-storage rate, lining structure characteristics and surrounding rock geological conditions are the influencing factors that cannot be ignored for the stability of the LRCs for CAES.

Moreover, deep natural rocks are composed of intact rocks and discontinuity surfaces such as weak interlayers and joints. These discontinuity surfaces play a leading role in the mechanical behaviors of rocks and give rise to a non-uniform stress distribution in rocks and therefore heterogeneous deformation (Gong et al. 2023; Ge et al. 2022; Wang et al. 2021; Li et al. 2023a, b). Meanwhile, operations are generally synchronized with construction in practical engineering, the blasting seismic waves affect the stress and deformation of LRCs under operation due to the compact layout and complex stacking of mine roadways (Salmi et al. 2019; Wang et al. 2022a, b, c; Zhang et al. 2019). Therefore, considering external factors such as weak interlayers, geostress, and blast load that affect LRCs for CAES, Zhang et al. (2021) assessed influences of uncoordinated deformation of surrounding rocks induced by the interlayers on stability of salt caverns for CAES. The results indicate that compared with hard interlayers, salt rocks and soft interlayers contribute more to the convergence of salt caverns. Zhang et al. (2017a, b) discovered that the top and bottom of layered salt caverns for CAES are more prone to shear failure, which has also been verified by numerical simulation. Wang et al. (2018a, b) believe that mudstone-interbedded salt caverns for CAES have poor seismic resistance under earthquakes, and the equivalent stress of the surrounding rocks near the interlayer is large. With increasing seismic amplitude, the plastic zone in the interlayer constantly expands. The above studies have fully considered the deformation and failure characteristics of the LRCs for CAES during the operation period, but there is little research into the stress characteristics of LRCs for CAES constructed by excavation and support of surrounding hard rock. There is also lack of research on stability of LRCs for CAES under joint

action of internal pressure, geostress, and weak interlayers during blasting in the adjacent cavern.

The research took a newly excavated tunnel-type LRC as the research object. By combining physical model tests and numerical simulation, influences of spatial distribution of weak interlayers on the stability of LRCs were investigated under joint action of internal pressure and blast load. The results provide useful engineering guidance for stability of LRCs for CAES under joint action of blast load and weak interlayers.

2 Similar model tests

2.1 Similarity law and materials

The physical model must be similar to the prototype in terms of its geometry, mass, load, physical properties of media, and boundary conditions (Wang et al. 2022a, b, c; Shi et al. 2015). According to dimensional analysis, the following conversion relations of various similarity constants can be obtained.

$$C_\sigma = C_l C_\gamma, \quad C_\sigma = C_\varepsilon C_E, \quad C_\mu = 1, \quad C_\delta = C_l C_\varepsilon, \quad C_\varphi = C_\sigma \tag{1}$$

where C_σ, C_l, C_γ, C_E, C_ε, C_μ, C_δ, and C_φ are the similarity ratios of stress, geometry, unit weight, elastic modulus, strain, Poisson's ratio, deformation, and internal friction angle, respectively.

The similarity ratios C_l and $C\gamma$ of geometry and unit weight in the tests are separately 80 and 1.44; the similarity ratios of the stress, cohesion, and elastic modulus are all 115; the similarity ratios of the Poisson's ratio, strain, and internal friction angle are all 1. Taking the reconstruction of an abandoned haulageway in a coal mine as a CRL for CAES as an example, the gas storage pressure reaches about 10 MPa. The ground elevation in the region of the coal mine is 900–1100 m, the burial depth of the roadway top is about 200 m, and rocks in most tunnel section are compact and hard, being classified as Class III rocks. By conducting experiments on mix proportions, gypsum, quartz sand, barite powder, and water were mixed at a ratio of 1:4:6:2.6 to prepare the similar material for simulating surrounding rocks. Gypsum, barite powder, powdered talc, and water were mixed at a ratio of 1:14.4:9.6:7.5 to prepare the similar material for simulating the weak interlayer. In addition, gypsum, barite powder, powdered talc, and

water were mixed at a ratio of 1:7.5:2.5:3.9 to prepare the similar material for simulating the lining. By comparing laboratory test results of polymer materials including AB mixed epoxy resin (three types: soft, medium, and hard), silica gel, and heat-shrinking polyolefin tubes, heat-shrinking polyolefin tubes best conform to the elastic modulus of the similar material needed for the sealing layer. Detailed mechanical parameters of the similar materials are listed in Table 1.

2.2 Physical model and test methods

2.2.1 Preparation of the physical model

In engineering practice, the design sizes of the LRC diameter, lining thickness, thickness of the sealing layer, and thickness of the weak interlayer were separately 8.0, 0.4, 0.03, and 0.8 m. According to the similarity law, the LRC diameter, lining thickness, thickness of the sealing layer, and thickness of the weak interlayer in the physical model were separately determined to be 100 mm, 5 mm, 0.38 mm, and 10 mm. Two conditions were considered in the laboratory tests: intersection of the weak interlayer with the LRC and separation of the weak interlayer from the LRC. Moreover, the condition without a weak interlayer was also set as the control group.
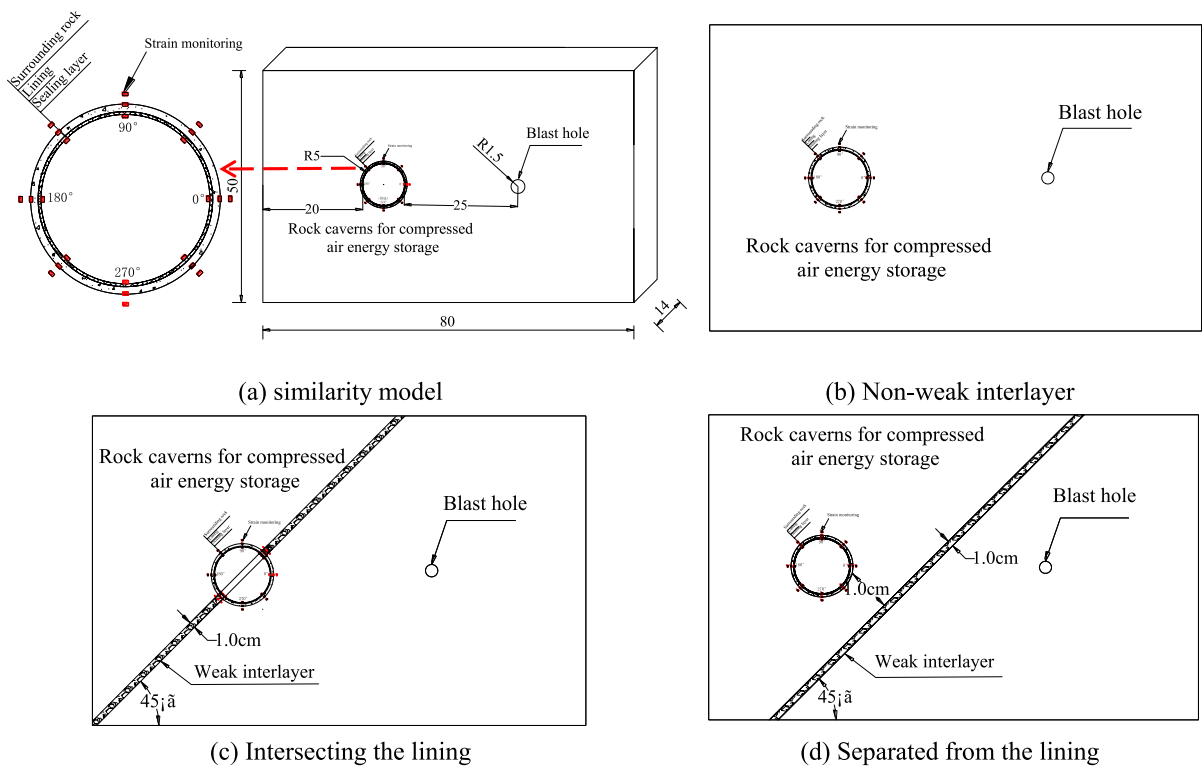
When the weak interlayer was intersected with the LRC, the interlayer passed through the center of the LRC; when the interlayer was separated from the LRC, the distance between the interlayer and the LRC boundary was 0.2 times of the LRC radius, with the dip angle of the interlayer being 45°. Details are illustrated in Fig. 1. A Donghua DH5960 hyperdynamic signal test and analysis system was used in the tests to collect strain data dynamically. It was adopted for real-time monitoring of circumferential strains of the sealing layer, lining, and surrounding rocks of the LRC for CAES. The strain gauges were arranged circumferentially along the LRC with an interval of 45°. Strain gauges were arranged more densely at the weak interlayer, as shown in Fig. 1a.

2.2.2 Confining pressure loading device

Relevant statistical data of geostress (Zhang et al. 2015) show that the horizontal and vertical geostresses at the LRC for CAES in the engineering

Table 1 Mechanical parameters of similar materials

Type	Volumetric weight (kN/m^3)	Elasticity modulus (GPa)	Compressive strength (MPa)	φ (°)	C (MPa)
Surrounding rock					
Parameter	26.5–28.3	35.3–31.3	36.2–60.4	22.0–30.6	7.9–9.5
Target value	18.4–19.6	0.3–0.27	0.265–0.516	22.0–30.6	0.680–0.820
Test value	18.2	0.306	0.75	34	0.062
Weak interlayer					
Parameter	20.0–23.0	1.3–6.0	0.30–0.35	27.0–39.0	0.2–0.7
Target value	14.3–16.4	0.01–0.05	0.3–0.35	27.0–39.0	0.0017–0.006
Test value	15.71	0.04	0.05	32	0.009
Concrete lining					
Parameter	26.0	30.0	0.18	55.0	3.2
Target value	18.0	0.26	0.18	55.0	0.028
Test value	17.96	0.256	0.38	45	0.035
Sealing layer					
Parameter	14.0–21.0	4.8	0.30	–	–
Target value	9.7–14.5	0.03	0.30	–	–
Test value	11.25	0.028	–	–	–

(a) similarity model

(b) Non-weak interlayer

(c) Intersecting the lining

(d) Separated from the lining

Fig. 1 Cavity model of compressed gas storage lining under adjacent cavity blasting

can be calculated using Eq. (2) to be 47 and 70 kPa, respectively. According to the similarity ratio, the initial geostresses in the model tests were obtained to be $\sigma_v = 0.047$ MPa and $\sigma_h = 0.070$ MPa, respectively.

$$\sigma_v = \gamma \cdot z, \sigma_h = \lambda \sigma_v \qquad (2)$$

where γ is the average unit weight of formations and is valued to be 27 kN/m^3; λ denotes the lateral pressure coefficient and is generally in the range of 0.8–1.5. Because the horizontal geostress is generally larger than the vertical geostress in shallow crusts, the lateral pressure coefficient is determined to be 1.5 here; z represents the burial depth of the LRC; σ_v and σ_h separately denote the vertical and horizontal geostresses.

To reproduce the geostress conditions encountered in engineering practice in laboratory physical model tests, a confining pressure loading device in Fig. 2 was designed. An F-shaped fixture was used to apply the confining pressure to the model. Strain gauges were pasted in the middle of the F-shaped fixture to measure the tensile force thereon, to control the clamping strength or confining pressure at boundaries of the model. Moreover, vibration-damping plates made of butyl rubber sheets were affixed to the inner side of surrounding rocks to absorb stress waves induced by blasting and therefore reduce influences of stress wave reflection on the boundaries. Outside the vibration damping plates is the force transfer structure formed by granite to ensure uniform diffusion

of the concentrated load generated by the F-shaped fixture. Finally, a polyvinyl chloride (PVC) thin layer and a grease coating were laid between the boundaries of the model and the vibration damping plates to decrease the friction force at boundaries. As a result, loads on boundaries were uniformly transferred to the model and the shear stress on the boundaries was removed.

2.2.3 Model pouring and test process

Taking the intersection model of the weak interlayer with the LRC in Fig. 3a as an example, PVC tubes with diameters of 100 and 30 mm were arranged in the pre-set LRC for CAES and the location of blasthole. In addition, two clamping plates at a spacing of 10 mm were arranged at the weak interlayer. The model pouring process is shown in Fig. 3b and c. Initial setting was finished in 20 min after pouring and the clamping plates of the weak interlayer were removed after 4 h, followed by pouring the weak interlayer. Finally, three models, that is, a model without the weak interlayer, a model in which the interlayer was intersected with the LRC, and a model in which the interlayer was separated from the LRC were established. Cylindrical gasbags were used in the tests to apply uniform pressure to the inner walls of the LRCs. The gasbags had the same size as the reserved LRCs in the models. In the tests, grease was smeared onto the gasbag surface to reduce friction between the gasbag and the LRC, thus decreasing the
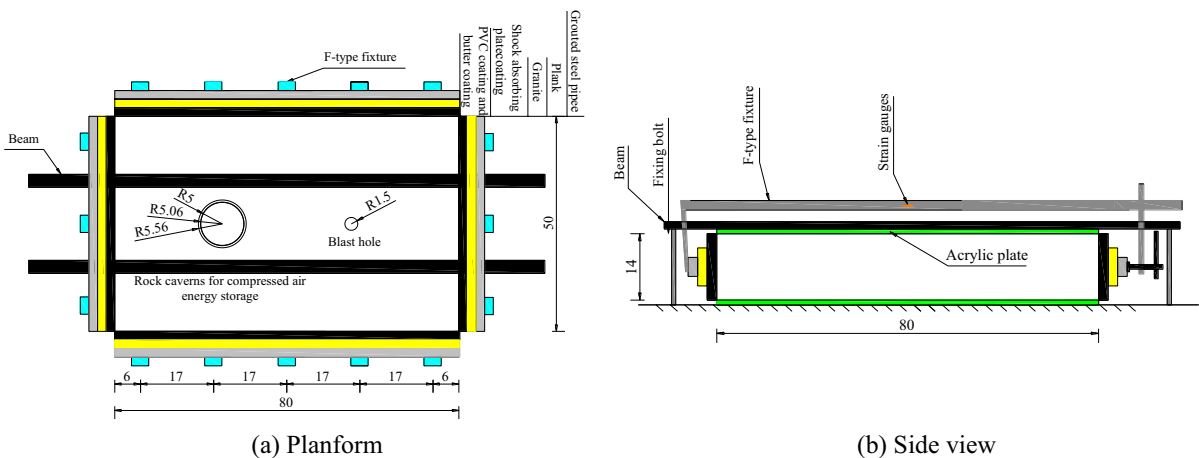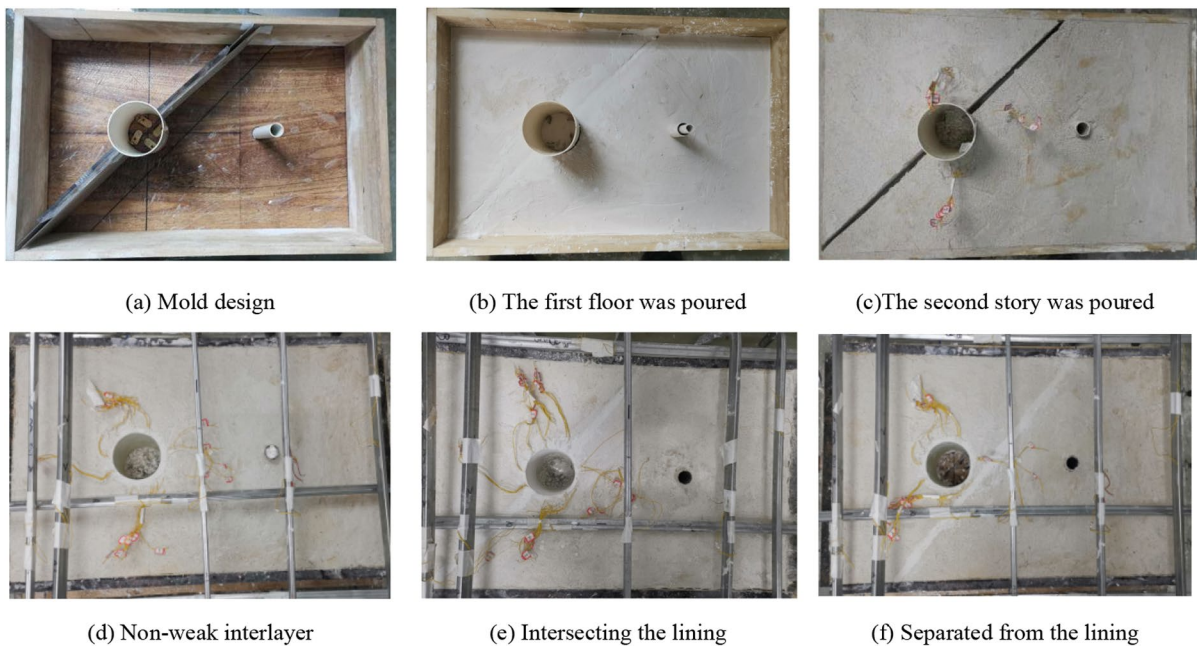

(a) Planform   (b) Side view

Fig. 2 Confining pressure loading device

(a) Mold design   (b) The first floor was poured   (c)The second story was poured

(d) Non-weak interlayer   (e) Intersecting the lining   (f) Separated from the lining

Fig. 3 Model pouring

tests error. The gasbags were made of rubber, with the thickness and elastic modulus of 1 mm and 7.8 MPa, respectively.

2.3 Analysis of test results

2.3.1 Stability of the LRC under gas storage pressure

The designed maximum gas storage pressure of the LRC for CAES was 10 MPa, so the maximum gas storage pressure in the model tests was calculated to be 86.5 kPa following the similarity law. To simplify the loading process, the maximum gas storage pressure was set to be 90 kPa, and multi-level loading was applied in the gas storage and discharge processes. The load applied at each level was 10 kPa, the loading lasted for 15 s, and the load was held for 15 s after loading, to ensure stable stress on surrounding rocks. Taking the model with a weak interlayer separating the cavity from the LRC as an example, the deformation characteristics of the sealing layer, lining, and surrounding rocks under different gas storage pressures are illustrated in Fig. 4. In the gas storage stage, the circumferential strain at various monitoring points nearly linearly increases with increasing gas storage pressure. The strain at the monitoring point with an

orientation of 315° nearest the interlayer grows most rapidly. As the distance from the interlayer increases, the rate of change of strain decreases at monitoring points with different orientations as the gas pressure increases. In the gas discharge stage, the circumferential strains at monitoring points at different positions decrease in a quasi-linear manner with decreasing gas storage pressure.

Under the maximum gas storage pressure, the maximum circumferential strain was recorded at the monitoring point (315°) near the weak interlayer. As the distance from the weak interlayer increases, the circumferential strain gradually decreases. The differences in circumferential strains of the sealing layer, lining, and surrounding rocks at monitoring points nearest (315°) and farthest (135°) to the interlayer are separately 112, 121, and 139 $\mu\varepsilon$. After discharging gas, the sealing layer, lining, and surrounding rocks all have residual strains, which are distributed in a shape protruding towards the weak interlayer. Various structures are listed in a descending order as the sealing layer, lining, and surrounding rocks according to their maximum residual strains. This suggests that the presence of the weak interlayer increases the overall tensile strain in regions near the weak interlayer in the LRC and it induces greater residual deformation
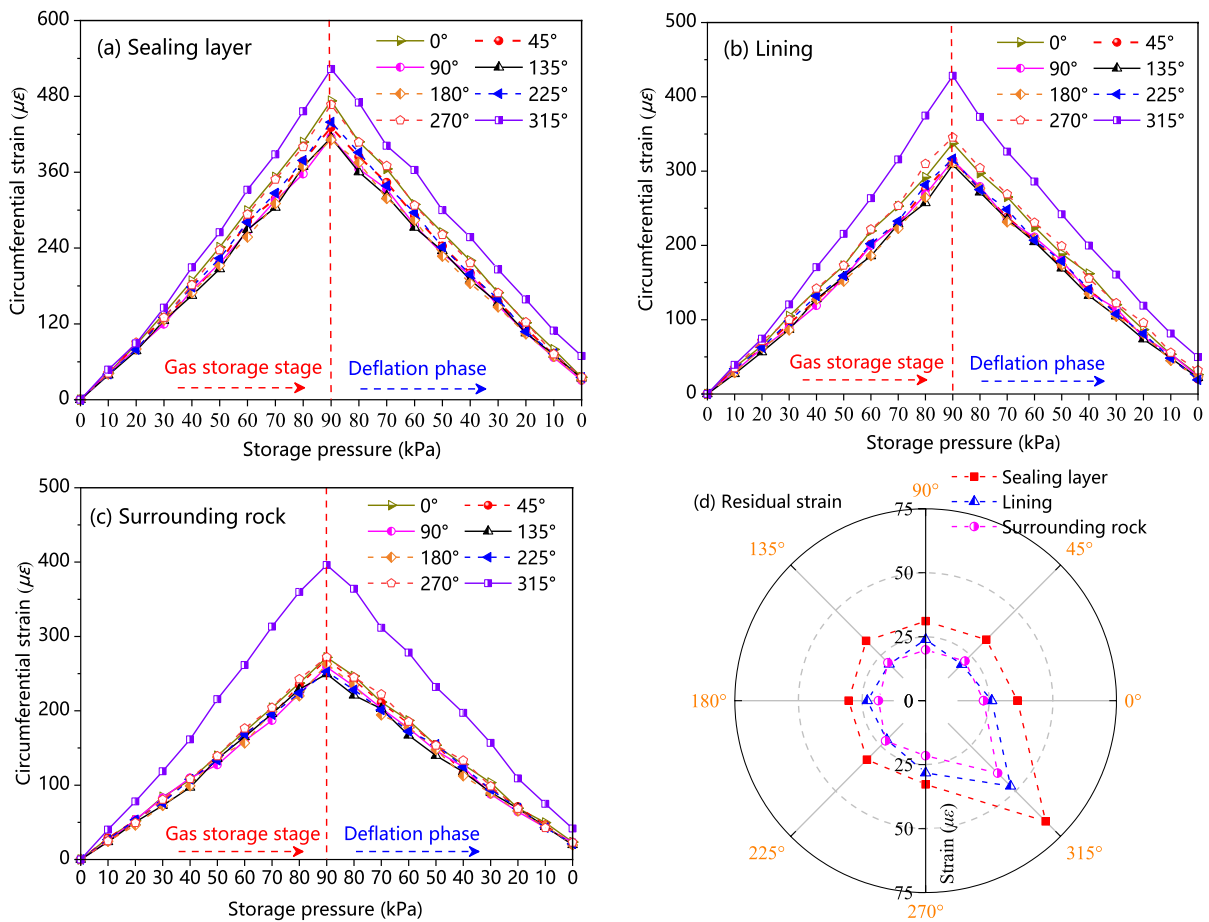
Fig. 4 Relationship between gas storage pressure and circumferential strain

after gas discharge, thereby affecting the stability of regions near the interlayer in the LRC.

The above analysis indicates that the presence of the weak interlayer induces a significant stress concentration in local areas of the LRC, thus generating significant tensile strain. Furthermore, the gas storage pressure is maintained at 90 kPa to compare strains in the LRCs under different conditions pertaining to the weak interlayer (Fig. 5). When the weak interlayer is intersected with the LRC, the interlayer influences the tensile deformation of the LRC (albeit to within a limited extent in a small region near the interlayer). The circumferential strains at various positions beyond the testing region of the weak interlayer are consistent with those in the case without the interlayer. At the soft-hard interface, the rate of changes in circumferential strains of the sealing layer and lining is as high as 105% and 150% (compared with those without the interlayer), while the circumferential strain of surrounding rocks does not increase to any significant extent. In the middle of the weak interlayer, the sealing layer has small compressive strain while the rate of changes in tensile strains in the outer layer of lining and the surrounding rocks is separately as high as 103% and 233%. After completely discharging gas, the residual circumferential strains of the sealing layer and lining grow by about 20 times at the intersection of the weak interlayer and surrounding rocks, while it does not increase in the surrounding rock. Under condition that the weak interlayer is separated from the LRC, the interlayer influences large areas of deformation in the LRC (mainly in the side facing the weak interlayer), which is also greatly affected by changes in the distance between the interlayer and the LRC; because the monitoring point at 315° has the shortest clear distance with the weak interlayer, the maximum

(a) Maximum strain

(b) Residual strain
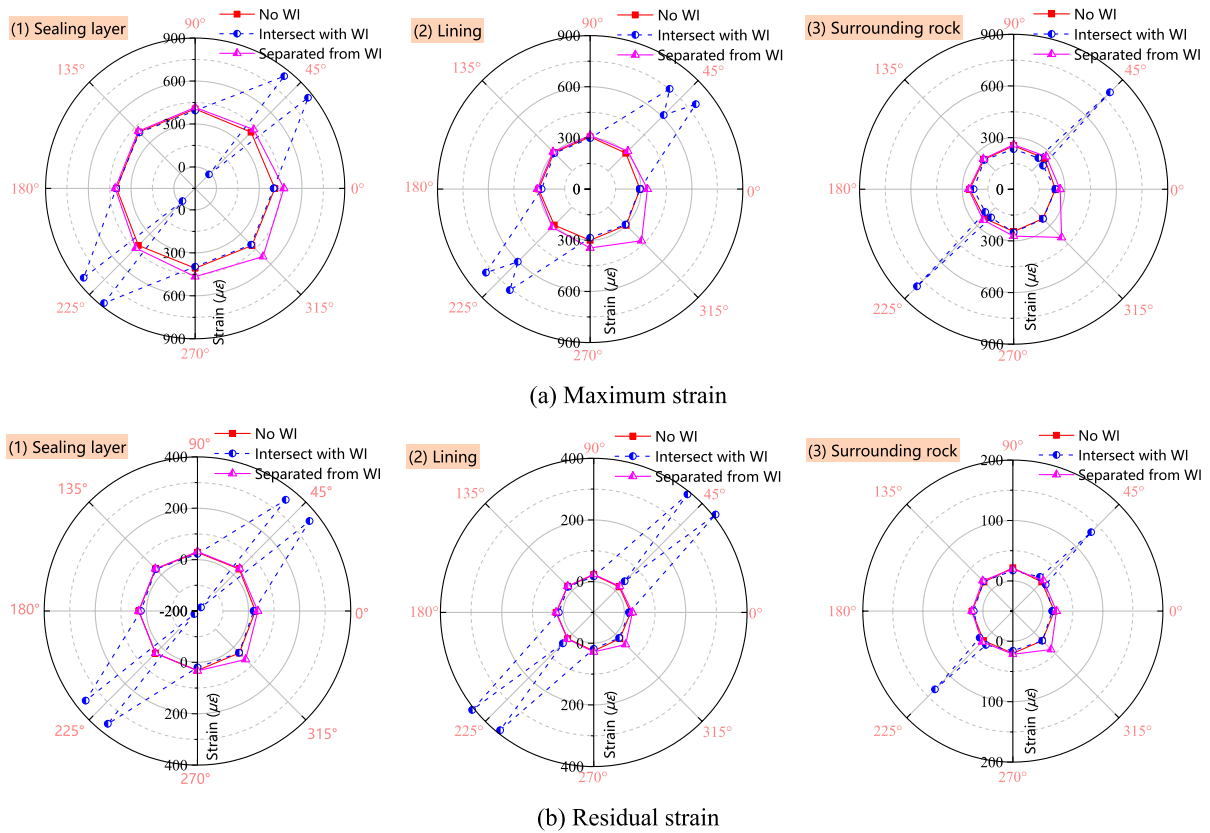
Fig. 5 Effect of gas storage pressure and weak interlayer on lining

rate of changes in circumferential strains of the sealing layer, lining, and surrounding rocks is separately 15%, 46.5%, and 51.7% compared with the condition without the weak interlayer.

The sealing layer is elastic and therefore it is not damaged in the test process, so the sealing layer was stripped from the surface of lining after tests to observe failure modes of the LRC under different conditions, as shown in Fig. 6. When the interlayer intersects with the LRC, the high gas storage pressure causes large changes in strain at the soft-hard interface, and the maximum strain reaches 800 µε. This is

Fig. 6 Influence of weak interlayer on failure pattern of lining cavity

(a) Intersect with weak interlayer

(b) Separated from weak interlayer
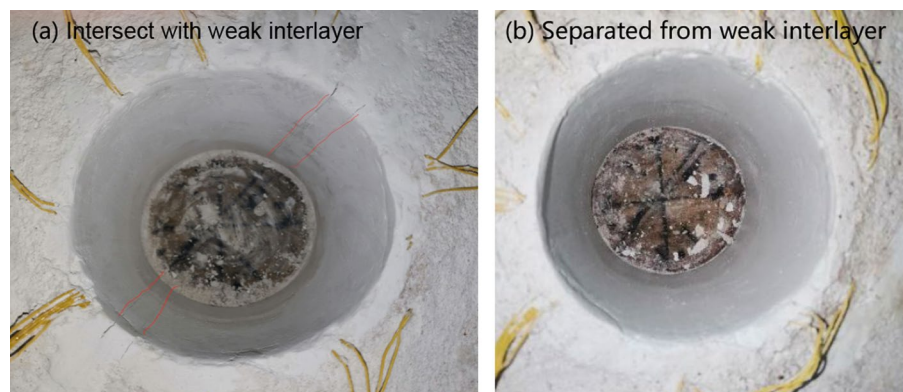
because the elastic modulus of the surrounding rock is higher than that of the weak interlayer, and the difference of elastic modulus leads to large deformation in the interface area under external load. At the same time, the performance of the transition interface area connecting the two media is relatively weak, which can easily cause slippage between the surrounding rock and the weak interlayer, and eventually inducing local damage to the lining and decreasing the bearing capacity of the LRC. If the interlayer is separated from the LRC, although the tensile strain in the lining near the interlayer is obviously greater than that of hard rocks, it still does not reach the cracking threshold of the lining, or the developed cracks are so small that they are closed after gas discharge.

2.3.2 Stability of the LRC during blasting in the adjacent cavern

Black powder was used in the laboratory tests to simulate the blast load. To select an appropriate explosive charge and therefore ensure generation of obvious dynamic responses in the LRC. The mass of the explosive charge was determined to be 6 g in the preliminary experiments. We found in preliminary experiments that when the explosive charge is 6 g, small cracks appeared around the blast hole (the extension length was within 2 cm), and the surrounding rock was in a stable state as a whole. When the explosive charge is 2 g and 4 g, the vibration response of the surrounding rock is smaller. However, when the charge is 8 g, cross cracks appear around the blast hole, and the cracks extend longer. Because the model without the weak interlayer is symmetric, monitoring points within 0°–180° were selected to study characteristics of dynamic strain in the LRC under the blast load, as shown in Fig. 7a–c. Under the same blast load, time-history curves for the dynamic strains of the sealing layer, lining, and surrounding rocks evolve in the similar manner. The sealing layer, lining, and surrounding rocks are listed in descending order according to their strains. The deformation of the LRC firstly changes from circular to elliptic compressive deformation and then rebounds under the blast load. Therefore, the circumferential strain at various locations at 0° and 180° firstly increases, then decreases, while the strain at other monitoring points first decreases, then increases. As shown in Fig. 7d, at the sealing

layer, the peak strains at monitoring points from 0° to 135° gradually reduce from 82 to 51 $\mu\varepsilon$ and it increases to 93 $\mu\varepsilon$ at the monitoring point at 180°. The distribution of peak strains of the lining and surrounding rocks is like that of the sealing layer on the whole. The peak strain decreases uniformly from monitoring points in the sealing layer to those in the surrounding rocks except for two testing regions at 0° and 180°. This indicates that the tensile failure of left and right-side walls of the LRC should be controlled when a blast load is applied to the right-hand side of the LRC.

Furthermore, characteristics of peak dynamic strains under three conditions are compared: without the weak interlayer, intersection of the weak interlayer with the LRC, and separation of the weak interlayer from the LRC, as shown in Fig. 8. In the case that the interlayer is intersected with the LRC, strains on the soft-hard interfaces in the sealing layer and lining increase compared with those without the interlayer. In addition, strain in the lining increases by more than that in the sealing layer. When the blasting stress waves do not propagate through the interlayer, strain of the lining within the testing region in 0°–270° (anticlockwise) is slightly affected by the interlayer, while that of the lining that passes through the interlayer (90°–180°, anticlockwise) increases apparently. When the interlayer passes through the center of the LRC, regions near the interlayer are easily damaged under the blast load. The influence extents at the interlayer are listed in descending order in surrounding rocks, lining, and sealing layer.

If the interlayer is separated from the LRC, peak strains of the sealing layer, lining, and surrounding rocks in the vicinity of the interlayer are all greater than those under the condition without the interlayer. In regions far from the interlayer, peak strains are obviously smaller than those under the condition without the interlayer. In the testing region at 315°, the closer to the interlayer, the more structures from the sealing layer to the surrounding rocks are affected by the interlayer. The weak interlayer exerts two influences on the LRC: on the one hand, the presence of the interlayer increases the circumferential strain and stress in the stress process; on the other hand, the presence of the interlayer causes the energy loss in the propagation of a blasting stress wave.
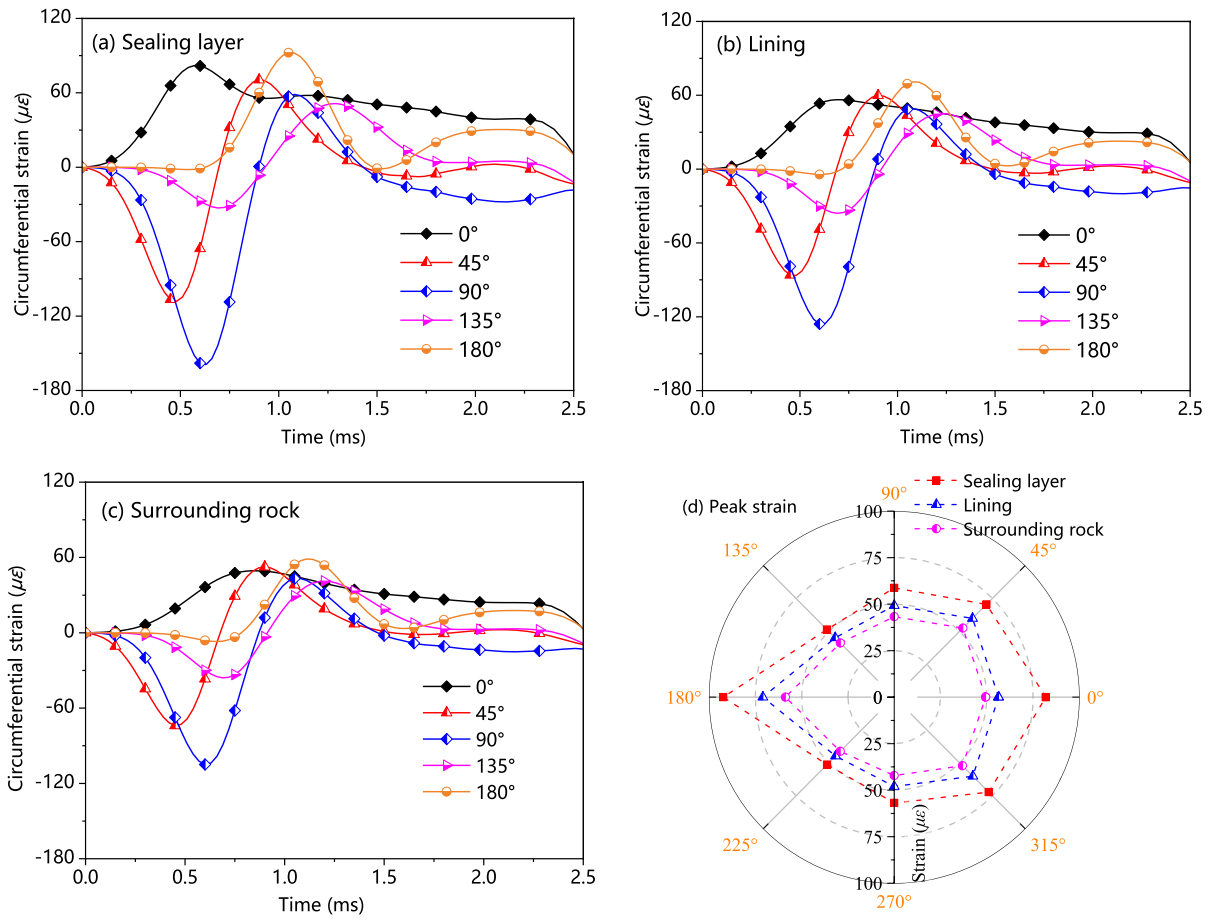
Fig. 7 Circumferential dynamic strain time history curve of lining without weak interlayers
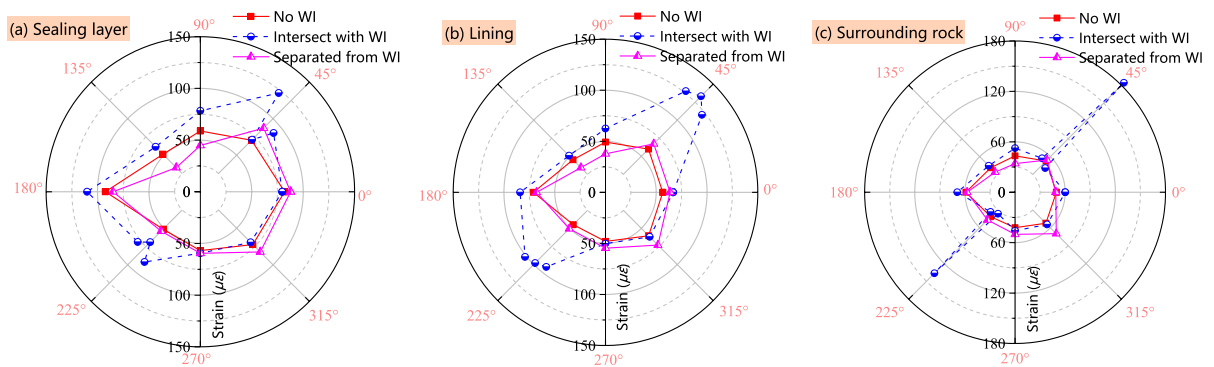
Fig. 8 Effect of explosion load and weak interlayer on lining deformation

3 Numerical simulation

3.1 Verification of laboratory tests by numerical simulation

To compare with the laboratory model test results, a two-dimensional (2-d) numerical model measuring 1000 mm×700 mm was established using COM-SOL Multiphysics, taking the separation of the weak interlayer from the LRC as an example, as shown in Fig. 9. The size of the surrounding rocks inside was 800 mm×500 mm, and infinite elements with the thickness of 100 mm were set around the periphery of the model to reduce stress wave reflection in the subsequent blasting process. The diameter of the lining in the LRC for CAES in the left side was 100 mm, and the thicknesses of the external sealing layer and lining were 0.38 mm and 5 cm. The pre-excavated adjacent cavern was set to leave a gap of 200 mm from the left LRC. The model contained 90,196 domain elements and 5673 boundary elements.

In the model, the Mohr–Coulomb strength criterion was applied to the weak interlayer and lining (Mebrahtu et al. 2022; Yang et al. 2022; Nian et al. 2023), while elastic constitutive was used to the

sealing layer. The material parameters were valued according to the experimental results of mix proportions of materials, as listed in Table 2. Uniform loads applied to the upper and right boundaries of the numerical model were separately 47 and 70 kPa, while normal displacement was limited in the lower and left boundaries.

As illustrated in Fig. 10, because the weak interlayer has a low wave impedance, the propagation of stress waves slows when passing through the interlayer. In addition, the stress wave energy attenuates to some extent, so the stress waves change abruptly when propagating through the interlayer. When the peak compressive stress waves pass through the LRC, the stress in the surrounding rocks near the interlayer increases, while those in the lining on the right-side wall and arch bottom differ slightly from those without the interlayer. Moreover, the stress in the vault reduces probably because the strain energy in the LRC is released at the interlayer; or the stress in the vault far from the interlayer decreases because the stress wave energy attenuates after passing through the interlayer. The stresses in the left side wall, right spandrel, and right arch foot all increase significantly when the tensile stress waves pass through the LRC.
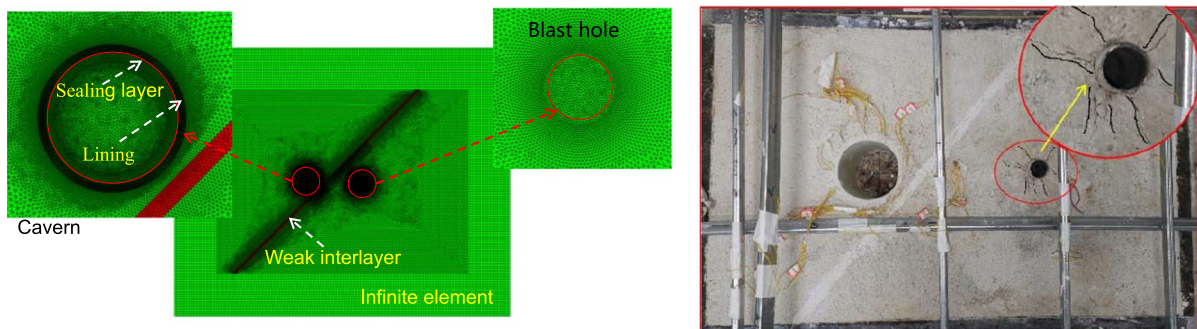

Fig. 9 Numerical model of compressed air energy storage test

Table 2 Mechanical parameters of similar model materials

Type	Parameter				
	Volumetric weight (kN/m^3)	Elasticity modulus (GPa)	φ (°)	C (MPa)	Poisson's ratio
Surrounding rock	18.2	305.8	34	0.062	0.26
Weak interlayer	15.7	40.6	32	0.009	0.3
Lining	18.0	255.8	45	0.035	0.18
Sealing layer	14.2	17.5	–	–	0.3

(a) 0.5ms   (b) 0.9ms   (c) 1.3ms
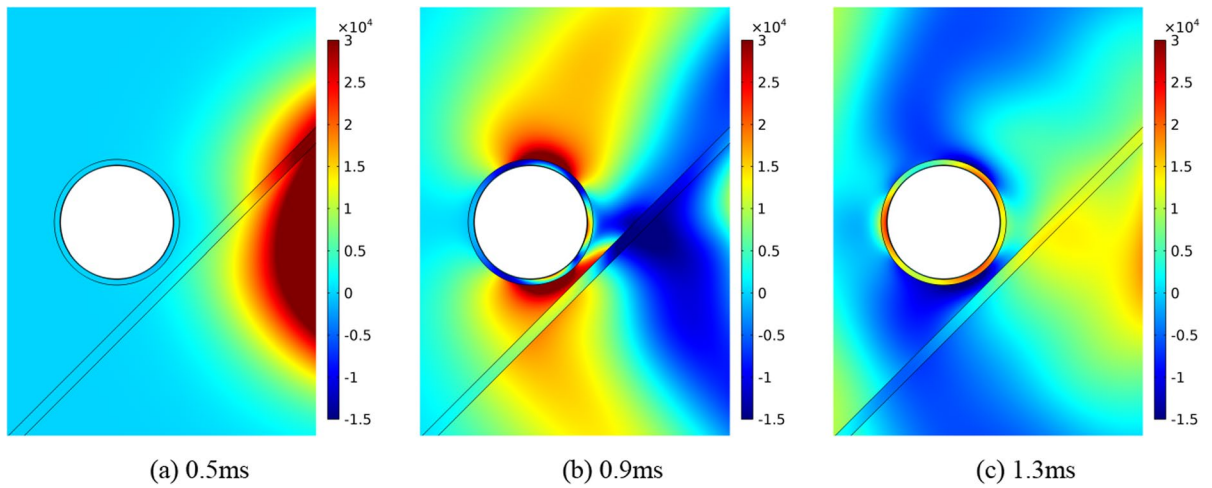
Fig. 10 Propagation path of explosion stress wave
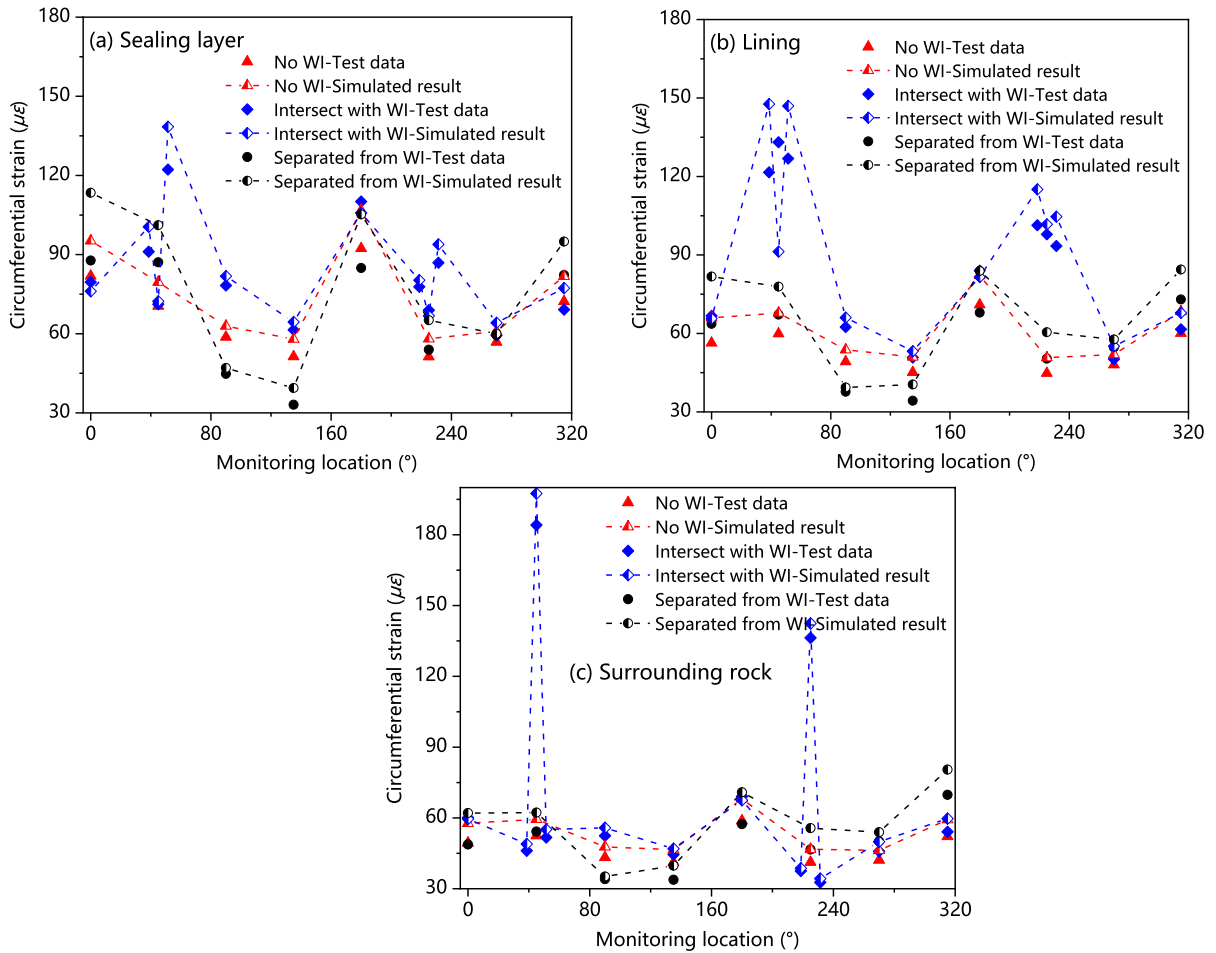
Fig. 11 Comparison of laboratory test and numerical simulation results

Furthermore, the laboratory model test results were compared with the numerical simulation results, as displayed in Fig. 11. Because the materials are somewhat idealized in numerical analysis, while there are some pores in test materials in which stress waves attenuate to a greater extent, the simulated results generally exceed those measured experimentally. Meanwhile, the blast load measured under the condition without the weak interlayer was used in numerical analysis. However in practical tests, the peak blast load under intersection of the interlayer with the LRC is slightly larger than that without the interlayer, and the measured blast load when the interlayer is separated from the LRC is slightly lower than the load used in the simulation. As a result, the calculated results differ from the measured values, whereas, the peak strains at various monitoring points under different conditions of the interlayer evolve quasi-consistently in numerical simulation and tests, which means that influences of the interlayer on the LRC revealed by the tests can be deemed reliable.

3.2 Full-scale numerical model of the LRC for CAES

Characteristics of strain in the LRC under gas storage pressure and influences of the weak interlayer were studied by conducting model tests. The possible failure locations and characteristics of the LRC were analyzed, which were also verified combining with numerical simulation. In practical engineering, the weak interlayer is distributed in a very uncertain manner. Differences in the thickness, dip angle, and relative location of the weak interlayer with the LRC for CAES all change the strain distribution in surrounding rocks under excavation

and gas storage pressure. This affects the stability of the LRC. Therefore, a full-scale numerical model was established to explore influences of different parameters of weak interlayers on strain in the LRC. The LRC diameter, lining thickness, and thickness of the sealing layer were 8 m, 0.4 m, and 30 mm, and the primary support of C25 plain concrete with a thickness of 80 mm was also considered in the calculation. According to the Saint–Venant's principle, the distance from the model boundary to the LRC boundary was set to be five times the LRC diameter to reduce the boundary effect. In the meantime, considering presence of a pre-excavated adjacent cavern at the position that was twice the LRC diameter to the right of the LRC in the initial stage, the finally designed finite element model measured 120 m × 88 m. Uniform loads of 5.4 and 8.1 MPa were separately applied to the upper and right boundaries of the model, while the normal displacement was limited on the lower and left boundaries. Values of the material parameters are listed in Table 3. The blast load was applied as the equivalent load to study the dynamic strain in the LRC. The semi-empirical and semi-theoretical formulae are commonly used in engineering practice, in which the time-history curves of blast load obtained by the double exponential function are widely utilized, while the coefficient needs to be determined according to actual measurement. According to previous research (Xu et al. 2022; Ji et al. 2021; Luo et al. 2022), the blast load can be simplified as triangular load, which shows fluctuations of the dynamic load. Considering this, the triangular load was adopted as the blast load in the research, which could be found, by calculation, to be $P_e \approx 24.8$ MPa using the calculation method for the equivalent load in (Yang et al. 2012).

Table 3 Different structural mechanical parameters

Type	Parameter				
	Volumetric weight (kN/m^3)	Elasticity modulus (GPa)	φ (°)	C (MPa)	Poisson's ratio
Surrounding rock	26.5	31.3	31	7.8	0.21
Weak interlayer	23.0	6.0	39	0.7	0.30
Preliminary bracing	26.0	29.5	54	2.7	0.20
Lining	26.0	30.0	55	3.2	0.18
Sealing layer	9.3	4.8	–	–	0.30

(a) 0MPa   (b) 2.5MPa   (c) 5MPa

(d) 7.5MPa   (e) 10MPa
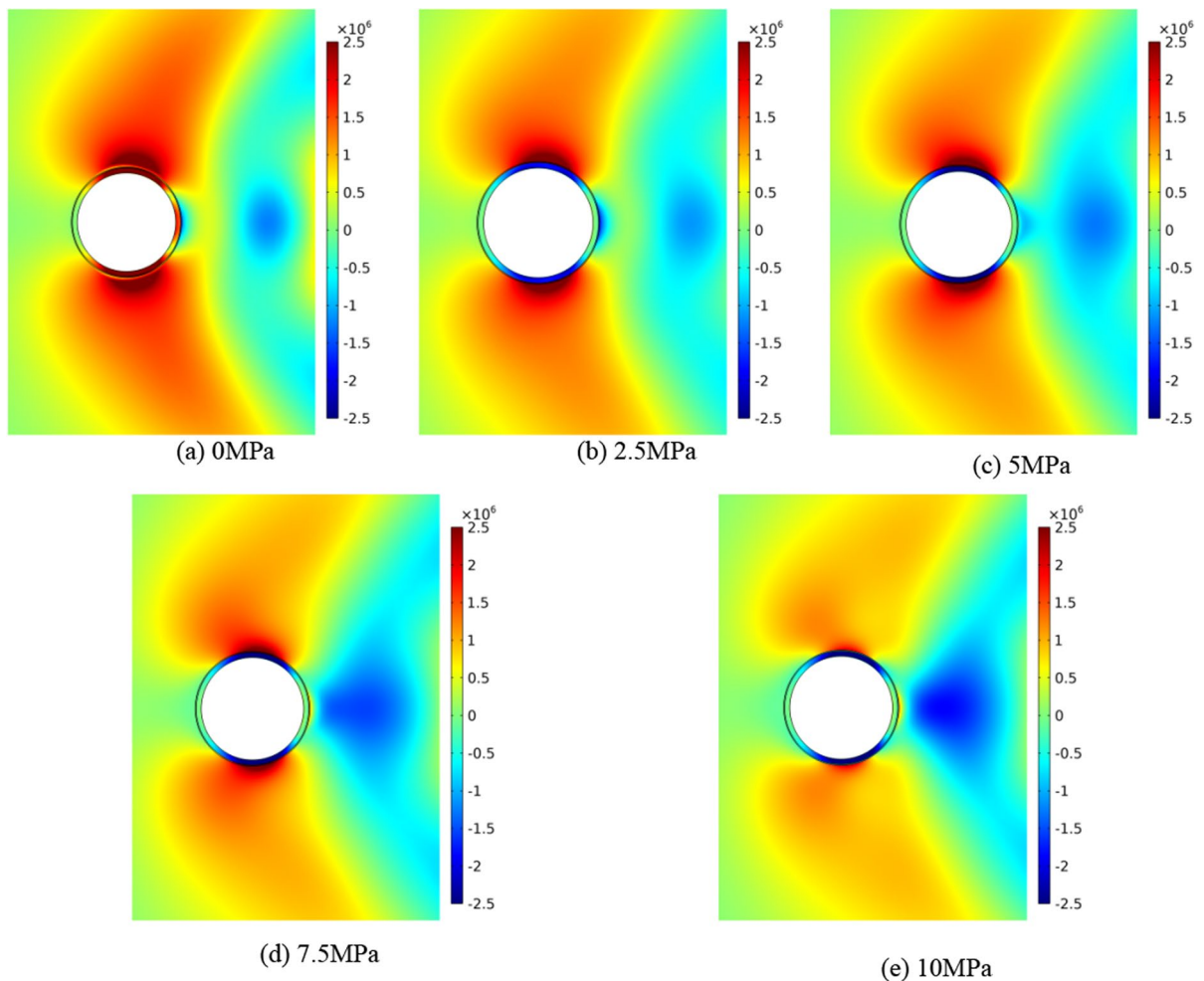
Fig. 12 Effect of gas storage pressure on lining stress increment

3.3 Influencing factors of stability of the LRC for CAES

#### 3.3.1 Influences of the gas storage pressure

Figure 12 presents the von Mises stress increment nephogram when the blasting stress waves propagate to the LRC. As the gas storage pressure increases, the stress increment in the rock surrounding the LRC decreases continuously. This is because when the gas storage pressure is 0, the circumferential stress of the surrounding rocks at the vault and arch bottom of the LRC is predominantly compressive. When the compressive stress waves produced by blasting propagate to the LRC, the action of the compressive stress is same as that of the initial compressive stress, so the total stress increases due to superposition of the two. However, the compressive stresses on surrounding rocks in the left and right-side walls of the LRC are low in the initial state and the propagation direction of blasting stress waves is vertical to the compressive stresses on the side walls, so certain tensile stress is generated to decrease the total stress. After the gas storage pressure rises to 2.5 MPa, the overall stress state of surrounding rocks is improved and the stress increment under the blasting stress waves is lower than the reduction of the pressure on the surrounding rocks under the gas storage pressure. Therefore, the blasting stress waves do not induce increments of the plastic strain of surrounding rocks any longer. Moreover, when the gas storage

pressure is 0, that is, the lining does not bear external force in the initial state, the overall stress on the lining increases under blasting stress waves, while the resultant force thereon is low, with a certain tensile stress found only in left and right-side walls. As the gas storage pressure increases to 2.5 MPa, the lining is circumferentially tensioned on the whole and it approaches (or has reached) yield. Under the blasting stress waves, the generated stress increment does not show obvious difference. If the gas storage pressure exceeds 2.5 MPa, the entire lining is in the

yield state, and the stress increment does not differ significantly under the blasting stress waves.

As shown in Fig. 13, the overall circumferential strains of the sealing layer, lining, and surrounding rocks follow a similar trend with the gas storage pressure under blasting stress waves. When the gas storage pressure exceeds 2.5 MPa, the increment of the gas storage pressure exerts only slight influences on the circumferential strain of the lining. When the gas storage pressure is 0, the circumferential strain at the vault reduces because the lining at the vault and arch bottom does not have undergo plastic deformation
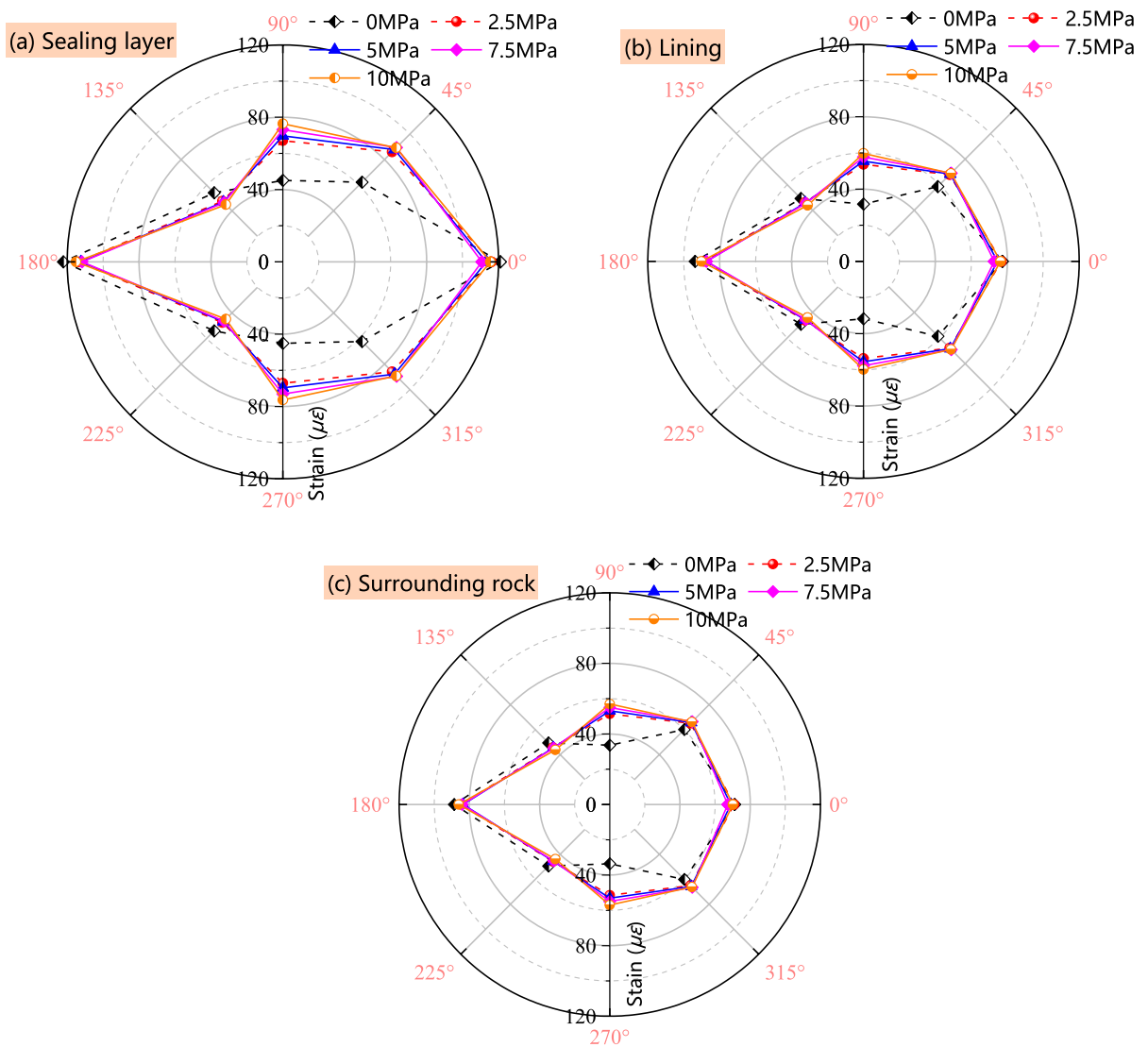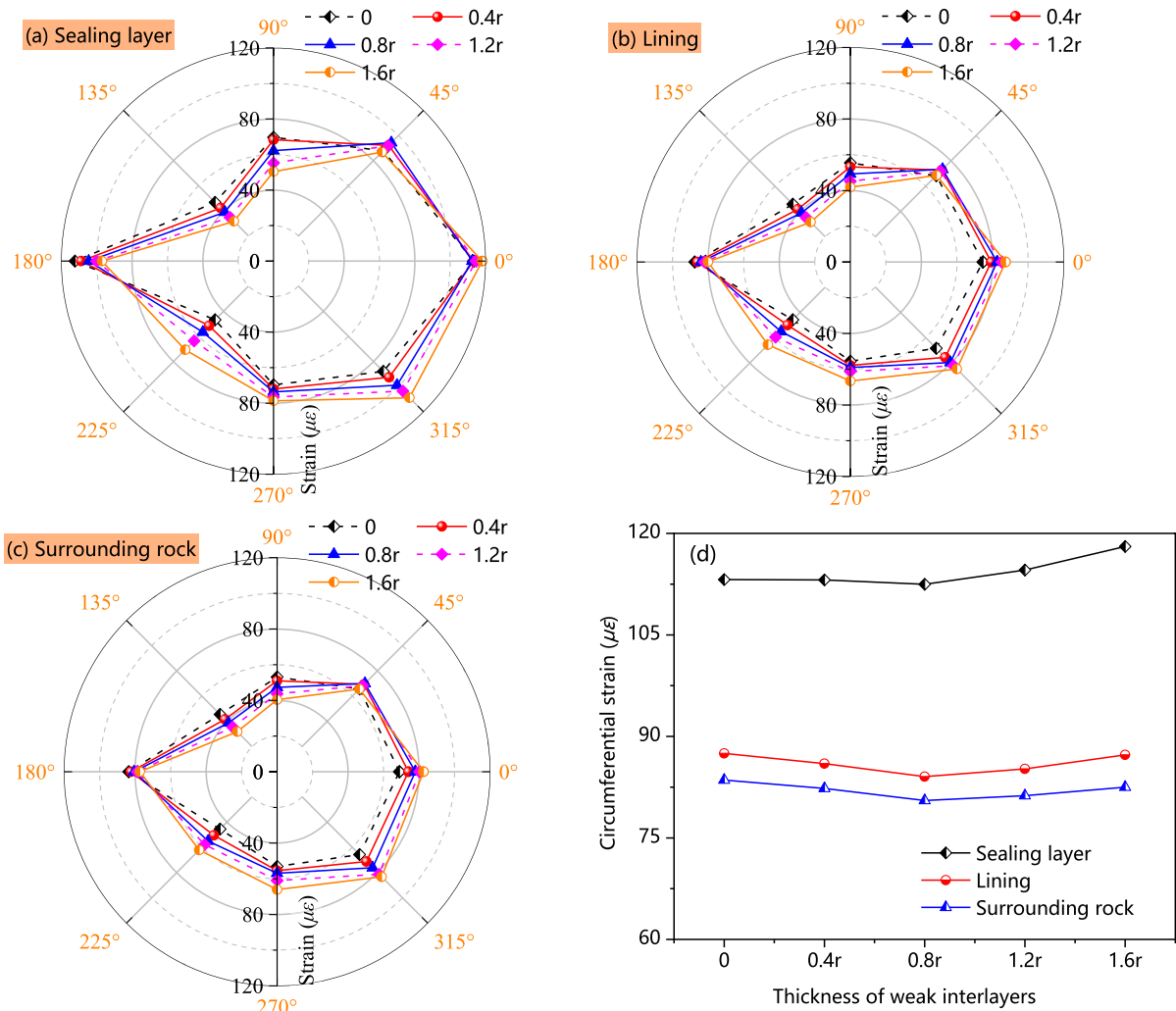

Fig. 13 Effect of gas storage pressure on circumferential strain of lining

under blast load and some energy is dissipated in the plastic deformation of the surrounding rock under compression. In both side walls, the peak strain varies a little under different gas storage pressures. Therefore, it can be judged from changes in the circumferential strain that the overall circumferential strain of the LRC is low under blasting stress waves when there is no gas storage pressure, and the increase in gas storage pressure not conducive to the stability of the LRC: because the presence of gas storage pressure alters the stress state of lining of the LRC for CAES, the lining is under a low stress if the gas storage pressure is low. Under blasting stress waves, the stress on the entire lining increases while the resultant force is low, and a certain tensile stress is generated only in the left and right-side walls. When the gas storage pressure is higher than 2.5 MPa, the lining is circumferentially tensioned and it approaches (or has reached) yield. In this case, the generated strain increment shows a slight difference under blasting stress waves.

3.3.2 Influences of the thickness of the weak interlayer

Under separation of the weak interlayer from the LRC, the distribution of the peak circumferential strains in the LRCs under conditions with different

Fig. 14 Effect of thickness of weak interlayer on circumferential strain of lining

thicknesses of the interlayer is shown in Fig. 14a–c. When the gas storage pressure is 5 MPa, the confinement of surrounding rocks at the interlayer on the LRC decreases with increasing thickness of the interlayer under the blast load. In the half LRC near the interlayer (45°–225°, anticlockwise), the circumferential strain always increases; while in the half of the LRC far from the interlayer, because the stress wave energy attenuates more with the increasing thickness of the interlayer, the peak strain reduces. The maximum peak strain of the sealing layer is found in the right-side wall; those of the lining and surrounding rocks appear in the left side-wall. Figure 14d illustrates the relationship between the thickness of the

weak interlayer and the maximum peak circumferential strain of the LRC. It can be seen from the figure that the maximum peak strains of the sealing layer, lining, and surrounding rocks under the condition do not significantly increase with the increasing thickness of the interlayer.

3.3.3 Influences of the dip angle of the weak interlayer

If the weak interlayer is separated from the LRC, distribution of the peak circumferential strains in the LRCs under different dip angles of the interlayer is illustrated in Fig. 15a–c. With the increase
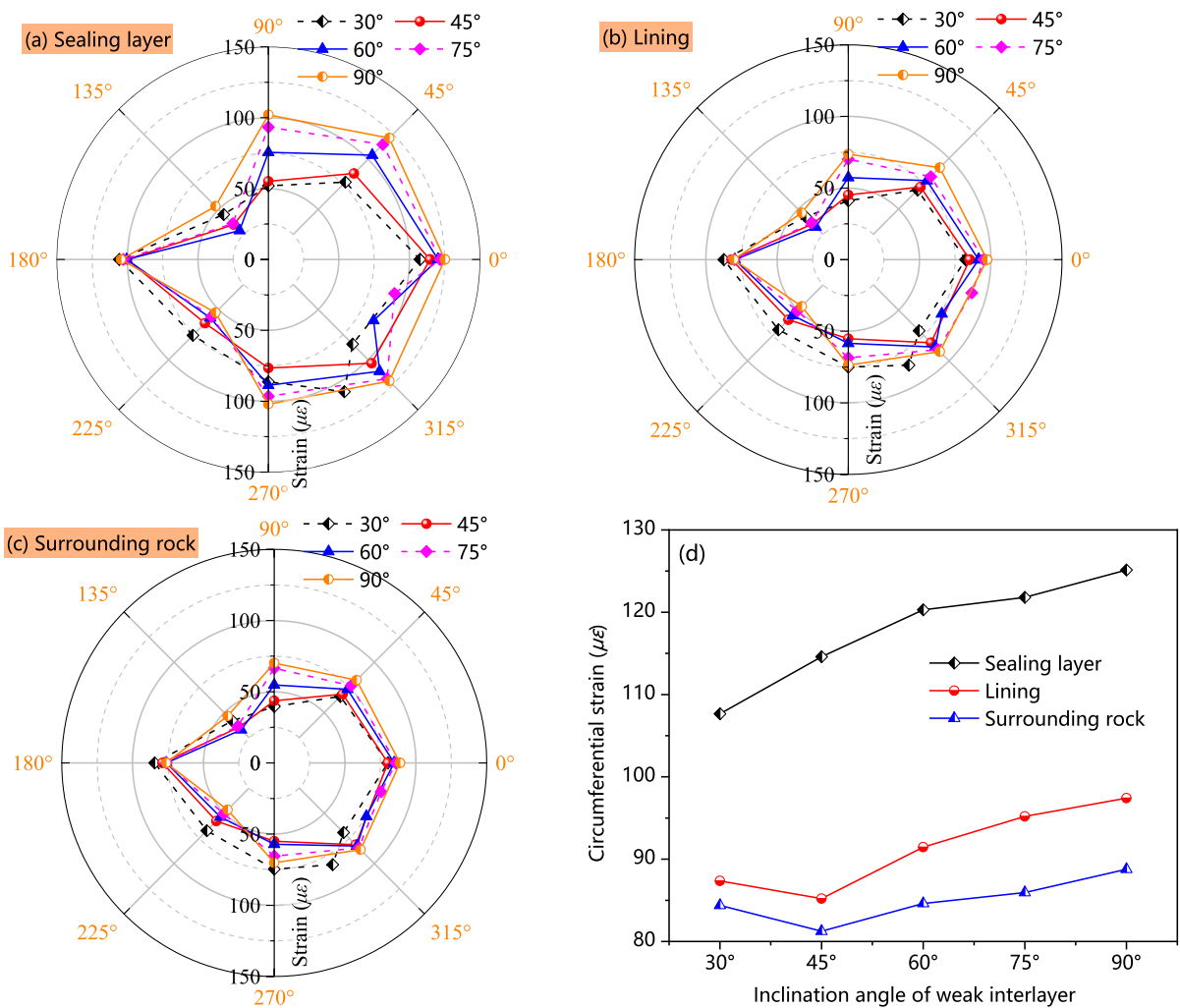

Fig. 15 Effect of Angle of weak sandwich on circumferential strain of lining

in dip angle, the peak strains in the right-hand parts (90°–315°, clockwise) of the sealing layer, lining, and rock surrounding the LRC are shown to all increase significantly and their ranges of influence also widen. Meanwhile, as the dip angle increases, the peak strains in some areas reduce relatively in the left parts (135°–270°, clockwise) of the sealing layer, lining, and surrounding rocks of the LRC that are further from the interlayer. The relationship between the dip angle of the interlayer and the peak circumferential strain of the LRC is displayed in Fig. 15d: as the dip angle increases, the maximum peak circumferential strain of the LRC increases slightly.

3.3.4 Influences of the location of the weak interlayer

Under separation of the weak interlayer from the LRC, distribution of the peak circumferential strains of the LRCs under different distances between the interface and the LRC boundary is illustrated in Fig. 16a–c. Variation of the distance between the interlayer and the LRC boundary affects the right arch foot of the LRC that is nearest to the interlayer to the greatest extent. As this distance increases, the peak strain at the right arch foot reduces significantly. Moreover, the peak strains at the right-side wall and the right spandrel also decrease. When the distance exceeds $0.1r$, the locations of peak circumferential
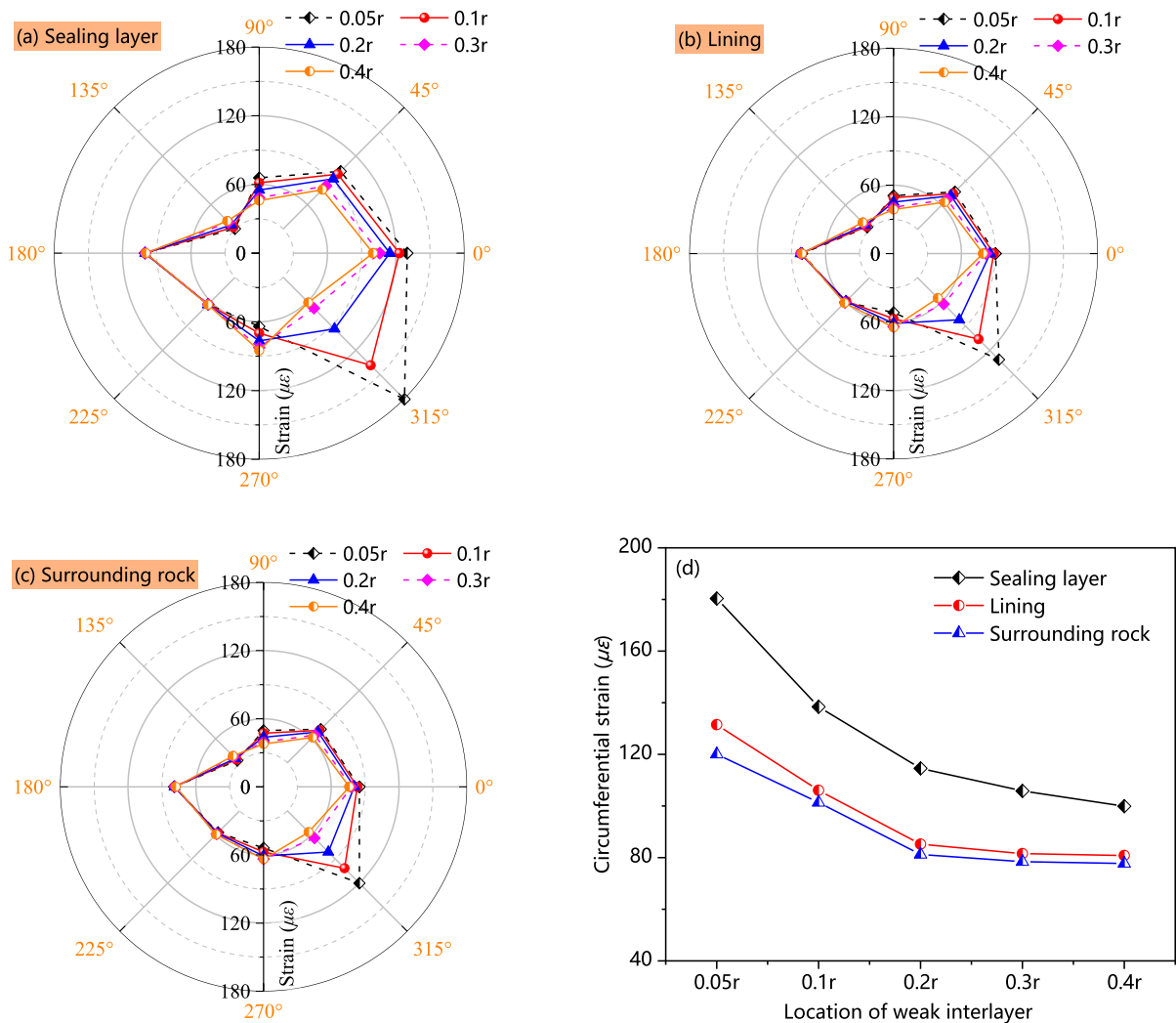
Fig. 16 Effect of sandwich position on circumferential strain of lining

strains of the sealing layer and lining shift from the right arch foot to the right-side wall. When the distance exceeds 0.2r, the location of peak circumferential strain of surrounding rocks shifts from the right arch foot to the right-side wall. Figure 16d display distribution of the peak circumferential strain in the LRC when the interlayer shows different distances to the LRC boundary; if the distance between the interlayer and the LRC boundary is less than 0.2r, the maximum peak strain in the LRC decreases significantly with increasing distance; when the distance exceeds 0.2r, the increment in the maximum plastic strain varies slightly as the distance increases.

4 Conclusion

Similar model tests for influences of blasting in the adjacent cavern on the LRC for CAES containing a weak interlayer were designed. The dynamic responses and deformation characteristics of the LRC for CAES under joint action of factors including the gas storage pressure, weak interlayer, and blast load were analyzed. Influences of the thickness, dip angle, and location of the weak interlayer on the deformation of the LRC were discussed. The following conclusions can be drawn:

1. In the gas storage stage of the LRC for CAES, the presence of the weak interlayer obviously accelerates the rate of change of strain in regions near the weak interlayer of the LRC with the rising gas storage pressure. The gas storage pressure exerts a greater influence on the sealing layer and lining than the surrounding rocks. The high internal pressure may cause irrecoverable deformation of the lining. The presence of the weak interlayer concentrates stresses in some parts of the LRC, increasing the circumferential and residual strains in the LRC;

2. Under the blast load, the time-history curves for dynamic strains of the sealing layer, lining, and surrounding rocks under the condition without the interlayer evolve in a similar manner, and large dynamic strains are found in both the left and right-side walls. The right-side wall of the LRC is least stable. The presence of the weak interlayer increases the circumferential stress on, and strain in, the LRC. As the gas storage pressure increases, the stress increment in surrounding rocks around the LRC constantly decreases. When the gas storage pressure increases to 2.5 MPa, the increment in gas storage pressure only slightly affects the circumferential strain in the lining. As the blasting stress waves propagate, the presence of the weak interlayer causes the energy loss in the propagation process of stress waves and increases the peak strain in regions near the interlayer of the LRC;

3. Under the blast load, if the weak interlayer is separated from the LRC, as the thickness of the interlayer increases, the surrounding rocks exert lower confinement on the LRC and the peak circumferential strain increases in the side of the LRC near the interlayer; in the side far from the interlayer, the increased thickness of the interlayer intensifies attenuation of stress waves and reduces the peak circumferential strain. As the dip angle of the interlayer grows, the further the interlayer from the left part of the LRC is, the lower the corresponding peak strain, while the peak strain in the upper right side of the LRC increases significantly. With the increase in the distance from the weak interlayer to the LRC boundary, the peak circumferential strain decreases at the right-hand arch foot of the LRC that is near the interlayer. When the distance is less than 0.2r, the increase in the distance significantly affects the peak strain.

Author contributions MZ: Data curation, Methodology, Writing—original draft. YL: Conceptualization, Methodology, Visualization, Formal analysis, Funding acquisition. HG (Corresponding author): Formal analysis, Writing-review and editing, Funding acquisition. XL: Conceptualization, Methodology, Visualization. YD: Writing-original draft, Data curation, Investigation.

Data availability The data that support the findings of this study are available from the corresponding author upon reasonable request.

Declarations

Ethics approval   Not applicable.

Consent for publish   All authors have confirmed the publication of this article.

Conflict of interest   We declare that there are no known competing financial interests or personal relationships that could have appeared to influence the work reported in this paper.

References

Carranza-Torres C, Fosnacht D, Hudak G (2017) Geomechanical analysis of the stability conditions of shallow cavities for Compressed Air Energy Storage (CAES) applications. Geomech Geophys Geo-Energy Geo-Resour 3:131–174

Chen XH, Wang JG (2022) Stability analysis for compressed air energy storage cavern with initial excavation damage zone in an abandoned mining tunnel. J Energy Storage 45:103725

Ge YM, Cao B, Tang HM (2022) Rock discontinuities identification from 3D point clouds using artificial neural network. Rock Mech Rock Eng 55:1705–1720

Geissbühler L, Becattini V, Zanganeh G, Zavattoni S, Barbato M, Haselbacher A (2018) Pilot-scale demonstration of advanced adiabatic compressed air energy storage, part 1: plant description and tests with sensible thermal-energy storage. J Energy Storage 17:129–139

Gong HL, Wang G, Luo Y, Li XP, Liu TT, Song LB, Wang XK (2023) Shear fracture behaviors and acoustic emission characteristics of granite with discontinuous joints under combinations of normal static loads and dynamic disturbances. Theor Appl Fract Mech 125:103923

Han Y, Ma HL, Yang CH, Li H, Yang J (2021) The mechanical behavior of rock salt under different confining pressure unloading rates during compressed air energy storage (CAES). J Pet Sci Eng 196:107676

Ji L, Zhou CB, Lu SW, Jiang N, Li HB (2021) Modeling study of cumulative damage effects and safety criterion of surrounding rock under multiple full-face blasting of a large cross-section tunnel. Int J Rock Mech Min Sci 147:104882

Jiang ZM, Gan L, Zhang DX, Xiao ZZ, Liao JH (2023) Study on distribution characteristics and evolution law of liner cracks in underground cavern for compressed air energy storage. Chin J Geotech Eng 32:1124

Kim HM, Rutqvist J, Ryu DW, Choi BH, Sunwoo C, Song WK (2012) Exploring the concept of compressed air energy storage (CAES) in lined rock caverns at shallow depth: a modeling study of air tightness and energy balance. Appl Energy 92:653–667

Kim HM, Rutqvist J, Jeong JH, Choi BH, Ryu DW, Song WK (2013) Characterizing excavation damaged zone and stability of pressurized lined rock caverns for underground compressed air energy storage. Rock Mech Rock Eng 46(5):1113–1124

Li YS, Zhu JB, Han DY, Zhao R, Ma YK, Zhou T (2023a) Experimental study of the dynamic responses of surrounding jointed rock masses and adjacent underground openings and induced ground vibrations subjected to underground explosion. Tunn Undergr Space Technol 135:105060

Li P, Kang H, Zhu Q, Wu Y, Zhang J, Fan LY, Wang Z (2023b) Numerical and experimental investigations of concrete lined compressed air energy storage system. J Clean Prod 390:136153

Luo Y, Gong HL, Qu DX, Zhang XP, Tao YH, Li XP, Wan S (2022) Vibration velocity and frequency characteristics of surrounding rock of adjacent tunnel under blasting excavation. Sci Rep 12:8453

Mahlia TMI, Saktisahdan TJ, Jannifar A, Hasan MH, Matseelar HSC (2014) A review of available methods and development on energy storage; technology update. Renew Sust Energy Rev 33:532–545

Mebrahtu TK, Heinze T, Wohnlich S, Alber M (2022) Slope stability analysis of deep-seated landslides using limit equilibrium and finite element methods in Debre Sina area, Ethiopia. Bull Eng Geol Environ 81:403

Nian GQ, Chen ZH, Zhang LF, Bao M, Zhou ZH (2023) Three-dimensional stability analysis of unsaturated slopes under variable rainfall conditions using a numerical method. Bull Eng Geol Environ 82:59

Rutqvist J, Kim HM, Ryu DW, Synn JH, Song WK (2012) Modeling of coupled thermodynamic and geomechanical performance of underground compressed air energy storage in lined rock caverns. Int J Rock Mech Min Sci 52:71–81

Saedi G, Soleimani B, Samani B, Arzani A (2021) The interaction between faults and in-situ stress on the kinematic and subsurface natural fracture of Aghajari oilfield in southwest of Iran. J Petrol Sci Eng 208:109567

Salmi EF, Karakus M, Nazem M (2019) Assessing the effects of rock mass gradual deterioration on the long-term stability of abandoned mine workings and the mechanisms of post-mining subsidence: a case study of Castle Fields mine. Tunn Undergr Space Technol 88:169–185

Shi XM, Liu BG, Xiao J (2015) A method for determining the ratio of similar materials with cement and plaster as bonding agents. Rock Soil Mech 36:5

Sopher D, Juhlin C, Levendal T, Erlström M, Nilsson K (2019) Evaluation of the subsurface compressed air energy storage (CAES) potential on Gotland, Sweden. Environ Earth Sci 78:197

Wang GJ, Zhang L, Liu CK, Cai SX, Qi TC (2018a) Dynamic response of gas storage cave ruin bedded salt rock to earthquake. J Disaster Prev Mitig Eng 38:4

Wang TT, Yang CH, Chen JS, Daemen JJK (2018b) Geomechanical investigation of roof failure of China's first gas storage salt cavern. Eng Geol 243:59–69

Wang FL, Xia KW, Yao W, Wang SH, Wang CL, Xiu ZG (2021) Slip behavior of rough rock discontinuity under high velocity impact: experiments and models. Int J Rock Mech Min Sci 144:104831

Wang Q, Wang Y, He MC, Li SC, Jiang ZH, Jiang B, Xu S, Wei HY (2022a) Experimental study on the mechanism of pressure releasing control in deep coal mine roadways located in faulted zone. Geomech Geophys Geo-Energy Geo-Resour 8:50

Wang HX, Zhang B, Xu NX, Yu X (2022b) Stability analysis of anhydrite mine-out as an underground gas storage based on DEM and similarity theory: a case study. Bull Eng Geol Environ 81:99

Wang W, Pan Y, Xiao Y (2022c) Synergistic mechanism and technology of cable bolt resin anchoring for roadway roofs with weak interlayers. Rock Mech Rock Eng 55:3451–3472

Xie HP, Zhang K, Zhou CT, Wang JX, Peng Q, Guo J, Zhu JB (2022) Dynamic response of rock mass subjected to blasting disturbance during tunnel shaft excavation: a field study. Geomech Geophys Geo-Energy Geo-Resour 8:52

Xu P, Yang RS, Guo Y, Chen C, Yang Y, Zuo JJ (2022) Investigation of the interaction mechanism of two dynamic propagating cracks under blast loading. Eng Fract Mech 259:108112

Xue XR, Zhang K, Chen WM, Deng KW (2021) Experimental investigation and viscoelastic-plastic model for sandstone under cyclic tensile stress. Geomech Geophys Geo-Energy Geo-Resour 7:77

Yang JH, Xia YY, Chen ZZ, Chen D, Pei YY, Zhu WH (2012) Dynamic behavior of road high cutting rock slope under the influence of blasting for excavation. Prog Earth Planet Sc 5:25–31

Yang T, Selvadurai APS, Wang S (2021) The influence of seepage characteristics on the reliability of a tunnel roof under dynamic disturbances. Geomech Geophys Geo-Energy Geo-Resour 7:92

Yang Y, Liu F, Wu W (2022) Assessing slope stability with an improved 3D numerical manifold method. Rock Mech Rock Eng 55:6409–6423

Yu HS, Engelkemier SJ, Gençer E (2022) Process improvements and multi-objective optimization of compressed air energy storage (CAES) system. J Clean Prod 335:130081

Zhang YX, He YN, Yong X (2015) Rock mechanics. China Architecture and Building Press, Beijing

Zhang QY, Duan K, Jiao YY, Xiang W (2017a) Physical model test and numerical simulation for the stability analysis of deep gas storage cavern group located in bedded rock salt formation. Int J Rock Mech Min Sci 94:43–54

Zhang GM, Wang LG, Wu Y, Li YP, Yu SY (2017b) Failure mechanism of bedded salt formations surrounding salt caverns for underground gas storage. Bull Eng Geol Environ 76(4):1609–1625

Zhang XQ, Gong PL, Wang K, Li JZ, Jiang YL (2019) Characteristic and mechanism of roof fracture ahead of the face in an LTCC panel when passing an abandoned roadway: a case study from the Shenghua Coal Mine, China. Rock Mech Rock Eng 52:2775–2788

Zhang GM, Liu YX, Wang T, Zhang H, Wang ZS, Zhao CC, Chen XY (2021) Pillar stability of salt caverns used for gas storage considering sedimentary rhythm of the interlayers. J Energy Storage 43:69–72

Zhao JS, Feng XT, Jiang Q, Zhou YY (2018) Microseismicity monitoring and failure mechanism analysis of rock masses with weak interlayer zone in underground intersecting chambers: a case study from the Baihetan Hydropower Station, China. Eng Geol 245:44–60

Zhou Y, Xia CH, Zhou SW, Zhang PY (2018) Air tightness and mechanical characteristics of polymeric seals in lined rock caverns(LRCs) for compressed air energy storage(CAES). Chin J Rock Mech Eng 37(12):2685–2696

Publisher's Note Springer Nature remains neutral with regard to jurisdictional claims in published maps and institutional affiliations.